Title

Visualizing the Nanoscale Oxygen and Cation Transport Mechanisms during the Early Stages of Oxidation of Fe—Cr—Ni Alloy Using In Situ Atom Probe Tomography

Journal

Advanced Materials Interfaces, 9(20)

ISSN

2196-7350

Authors

Devaraj, Arun

Barton, Dallin J

Li, Cheng-Han

et al.

Publication Date

2022-07-01

DOI

10.1002/admi.202200134

ADVANCED MATERIALS INTERFACES
www.advmatinterfaces.de

Visualizing the Nanoscale Oxygen and Cation Transport Mechanisms during the Early Stages of Oxidation of Fe–Cr–Ni Alloy Using In Situ Atom Probe Tomography

Arun Devaraj, Dallin J. Barton, Cheng-Han Li, Sten V. Lambeets, Tingkun Liu, Anil Battu, Shutthanandan Vaithiyalingam, Suntharampillai Thevuthasan, Feipeng Yang, Jinghua Guo, Tianyi Li, Yang Ren, Libor Kovarik, Daniel E. Perea, and Maria L. Sushko*

Understanding the early stages of interactions between oxygen and material surfaces—especially at very high spatial resolutions—is highly beneficial for fields ranging from materials degradation, corrosion, geological sciences, forensics, and catalysis. The ability of in situ atom probe tomography (APT) is demonstrated to track the diffusion of oxygen and metal ions at nanoscale spatial resolution during the early stages of oxidation of a model Fe–Cr–Ni alloy. Using ^{18}O isotope tracers in these in situ APT experiments and complementary ex situ multimodal microscopy, spectroscopy, and computational simulations allows to precisely analyze the kinetics of oxidation and determine that outward cation diffusion to oxide/air interface is the primary mechanism for intragranular oxide growth in this alloy at 300 °C. This unique in situ isotopic tracer APT approach and the insights gained can be highly beneficial for studying early stages of gas–surface reactions in a broad array of materials.

1. Introduction

Understanding the oxidation mechanisms of solid materials and analyzing the resultant distribution of oxygen isotopes at nanoscale spatial resolution is pivotal to understanding of a wide variety of processes, including material degradation,[1–5] corrosion of engineered materials,[6–8] microorganism corrosion,[9] oxidation of anodes in solid oxide fuel cells,[10] and catalysis.[11,12] In geological sciences mapping ^{18}O in solid minerals is important for understanding the origin of Earth's crust formation[13–15] and magnetism.[16] In forensics, ^{18}O mapping in materials can be instrumental for tracing geographical origins of animals and humans.[17] Among the different methods used to study the oxidation mechanisms in solid materials, in situ environmental transmission electron microscopy (TEM) and in situ scanning tunneling microscopy are powerful for studying the atomic-scale structural changes associated with the early stages of oxidation.[1,3,5,18,19] However, these in situ techniques lack the sensitivity to distinguish individual oxygen isotopes. At the same time, nanosecondary ion mass spectrometry (SIMS) and other mass-spectrometry-based techniques, which are highly sensitive for oxygen isotopes, lack 3D sub-nanometer-scale spatial resolutions.[14,17,20,21] Recently, ex situ atom probe tomography (APT) studies validated the ability of APT to achieve sub-nanometer-scale spatially resolved mapping of ^{18}O isotope distribution in materials.[10,22–25] However, expanding this ability of APT in mapping ^{18}O quantitatively at sub-nanometer scale spatial resolution toward in situ oxidation studies is yet to be demonstrated.

Here, we demonstrate for the first time in situ APT analysis of oxygen diffusion in a model Fe–18 wt% Cr–14 wt% Ni model alloy (from here on called as Fe18Cr14Ni) using an ^{18}O isotopic

A. Devaraj, D. J. Barton, C.-H. Li, S. V. Lambeets, T. Liu, S. Thevuthasan, L. Kovarik, M. L. Sushko
Physical and Computational Sciences Directorate
Pacific Northwest National Laboratory
Richland, WA 99354, USA
E-mail: arun.devaraj@pnnl.gov

The ORCID identification number(s) for the author(s) of this article can be found under https://doi.org/10.1002/admi.202200134.

[+]Present address: Department of Physics, City University of Hong Kong, Kowloon, Hong Kong

A. Battu, S. Vaithiyalingam, D. E. Perea
Environmental Molecular Sciences Laboratory
Pacific Northwest National Laboratory
Richland, WA 99354, USA

F. Yang, J. Guo
Advanced Light Source
Lawrence Berkeley National Laboratory
Berkeley, CA 94720, USA

T. Li, Y. Ren[+]
Advanced Photon Source
Argonne National Laboratory
Lemont, IL 60439, USA

DOI: 10.1002/admi.202200134

tracer and an environmental reactor chamber attached to the APT system.[26–29] We chose an austenitic Fe–18 wt% Cr–14 wt% Ni alloy because of its importance as a model alloy for stainless steels, which are widely used in everyday life and engineering applications because of their excellent mechanical properties and corrosion resistance. Despite the excellent corrosion resistance of stainless steels in ambient conditions, in applications such as nuclear reactors, stainless steels are subjected to higher temperatures up to 360 °C in pressurized water environments, where issues such as stress corrosion cracking (SCC) become serious concerns.[30,31] In addition, a combination of oxidation and hydrogen-assisted degradation mechanisms can lead to catastrophic failure of stainless steels under such higher temperature corrosive conditions.[32] Therefore, developing comprehensive mechanistic models that can accurately predict the SCC failure of stainless steels has been a topic of significant research interest for decades.[31,33–36] For understanding the mass transport phenomena guided by a combined thermodynamic stabilization and stress relaxation that are ultimately responsible for SCC of stainless steels, it is important to first understand the initiation and propagation of oxidation at an atomic scale. Here, we provide 3D nanoscale compositional details of the oxide formed at 300 °C on the model austenitic alloy. Dual-step oxidation with $^{18}O_2$ exposure was used to confirm that outward diffusion of cations is ultimately responsible for oxide growth. In situ APT results were correlated with the multimodal analysis of the structure and oxidation state of the oxides formed by using ex situ TEM, X-ray photoelectron spectroscopy (XPS) depth profiling, and synchrotron-based X-ray absorption near edge spectroscopy (XANES). The nanoscale spatially resolved analysis accomplished by in situ isotopic tracer APT complements high-temperature ex situ oxidation studies on stainless steels and other materials to reveal the fundamental mechanisms underpinning the microstructure and property degradation in materials under extreme environments.

2. Results and Discussion

2.1. Model Alloy Microstructure

Fe18Cr14Ni was fully austenite stabilized with heat treatment at 900 °C for 4 h after cold rolling. The polycrystalline microstructure is seen in the electron backscatter diffraction band contrast map and inverse pole figure (IPF) in **Figure 1**a,b. Synchrotron based high energy X-ray diffraction further confirmed the fully austenite stabilized microstructure in the alloy (Figure 1c) where only face centered cubic (FCC) peaks are observed. Both IPF map and X-ray results show a random texture in the alloy suggesting that the rolling texture was completely removed on recrystallization and grain growth at 900 °C. APT needle samples prepared from the middle of grains revealed uniform distribution of Fe, Cr, and Ni at nanoscale spatial resolution (Figure 1d–f). The APT mass-to-charge spectra from the Fe18Cr14Ni alloy are given in Figure S1 in the Supporting Information. The

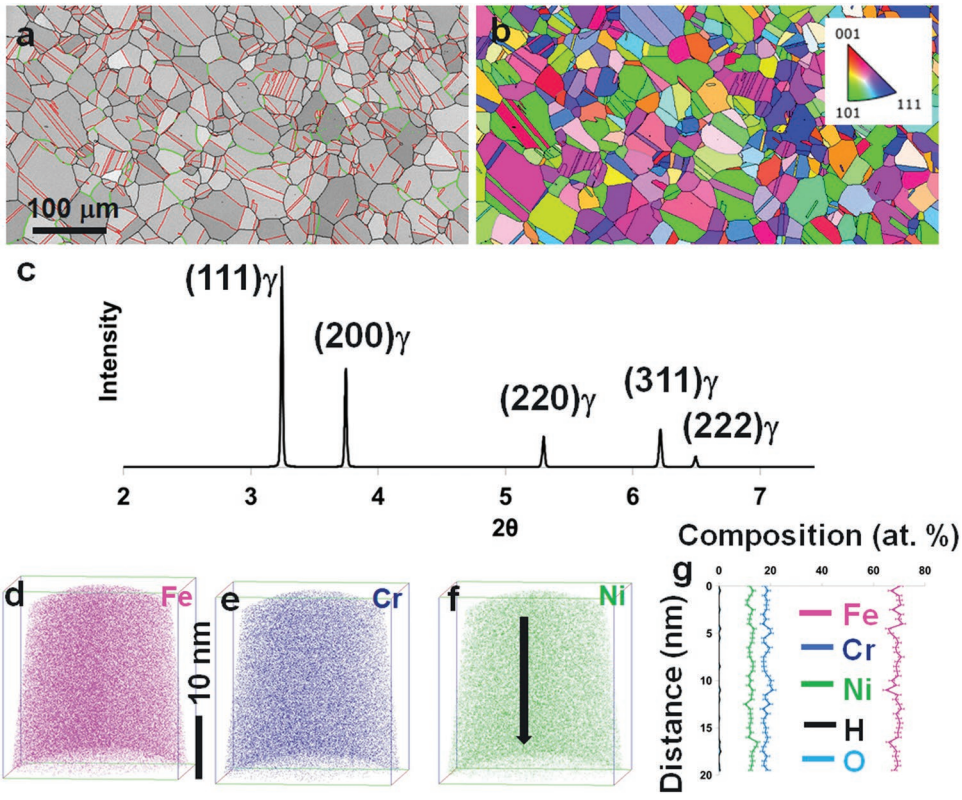

Figure 1. Model Fe18Cr14Ni alloy microstructure. a) Electron backscatter diffraction band contrast image with high angle grain boundaries highlighted in black, twins in red, and low angle grain boundaries in green and b) inverse pole figure of the Fe18Cr14Ni alloy. c) Synchrotron based high energy X-ray diffraction of Fe18Cr14Ni alloy confirming the fully austenite stabilized microstructure. Distribution of d) Fe, e) Cr, and f) Ni ions in the APT reconstruction showing uniform distribution of all elements. g) A 1D compositional profile showing that the elemental distribution is uniform along the length of the APT needle sample before oxidation in the reactor chamber.

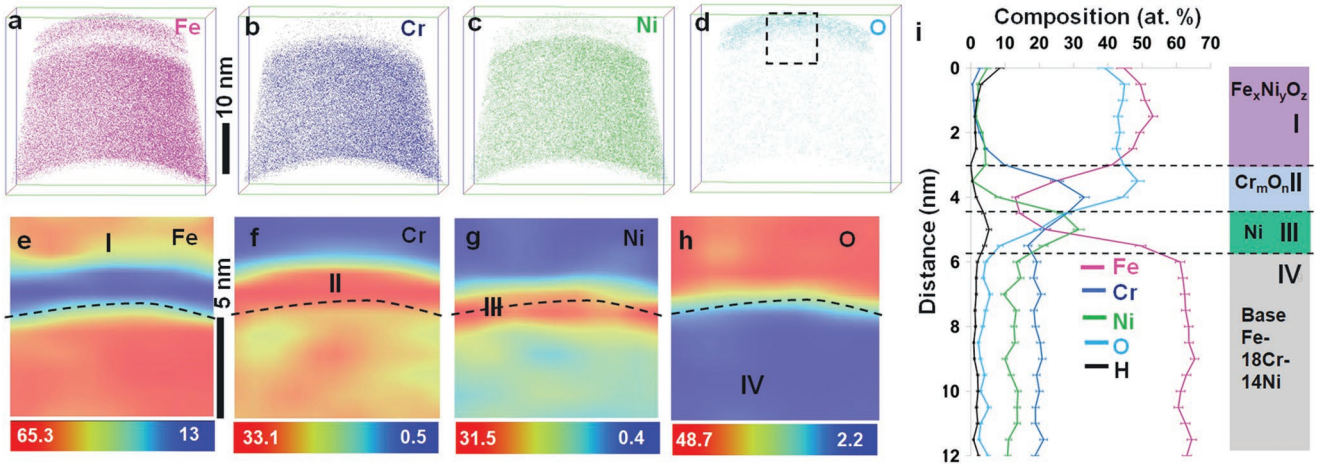

Figure 2. Oxide composition after 5 min oxidation at 300 °C in 10 mbar natural abundance O_2. Elemental distributions of a) Fe, b) Cr, c) Ni, and d) O revealed by APT after 300 °C, 5 min oxidation in natural-abundance oxygen. A $1 \times 10 \times 10$ nm^3 region of interest is marked by a dashed black rectangle from which 2D compositional maps were plotted to show the variation of e) Fe, f) Cr, g) Ni, and h) O across the oxide–metal interface. Individual, compositionally distinct regions in the oxide and base alloy are marked by numerals I–IV. The oxide–metal interface is demarcated using a dashed line in (e)–(h). i) 1D compositional profile showing the quantitative compositional changes from the oxide surface to the base alloy across the different layers.

mass-to-charge spectra peak overlaps between Fe, Cr and Ni isotopes were decomposed using counts of nonoverlapping isotopic peaks and known natural isotopic abundances as described in the Supplementary Information. The uniformity of Fe, Cr, and Ni distribution was additionally confirmed by a 1D composition profile along the axis of the APT reconstruction (Figure 1g). After an initial APT analysis and collecting ≈500 000 ions, the APT experiments were interrupted, and the needle samples were rapidly transferred in vacuum to a preheated reactor chamber attached to the APT buffer chamber. Once the samples reached 300 °C, the Fe18Cr14Ni needle samples were exposed to 10 mbar natural abundance O_2 for 5 min. After the 5 min oxidation, the needle samples were again transferred back into the APT analysis chamber to analyze the changes induced by the oxidation.

2.2. In Situ Atom Probe Tomography Oxidation Experiments with O_2

A 5 min exposure to natural abundance O_2 at 300 ° C considerably modified the near-surface composition of the Fe18Cr14Ni alloy needle samples. The comparison of APT mass-to-charge spectra before and after 5 min oxidation is shown in Figures S1 and S2 in the Supporting Information, where the new oxide peaks observed are indexed. From the mass-to-charge spectra after 5 min oxidation, in addition to the O^{+1} peak at 16 Da, an additional peak of OH^{+1} was noted at 17 Da and H_2O^{+1} was observed at 18 Da. The counts of the peaks at 17 and 18 Da were comparable. The distribution of Fe, Cr, Ni, and O in the APT reconstruction after oxidation is shown in **Figure 2**a–d, revealing formation of a multilayered oxide on the surface. A 2D concentration map was then extracted using a $1 \times 10 \times 10$ nm^3 region of interest near the top oxidized surface, denoted by the dashed rectangle in Figure 2d. The 2D concentration maps revealed the top surface oxide (denoted as I) with ≈2 nm thickness from the APT needle surface to be primarily rich in Fe (Figure 2e), depleted in Cr (Figure 2f), and with less Ni (Figure 2g). The second oxide layer (marked by II in Figure 2f) was a subsurface oxide with ≈1.5 nm thickness that was rich in Cr with significant depletion of Fe, where the oxygen concentration appeared to be the highest (Figure 2h). Layer III appeared to be an ≈1 nm thick region of Ni enrichment located at the oxide–metal interface indicated with a dashed line in Figure 2e–h. The unchanged base alloy composition (region IV) was observed only after the Ni-enriched layer III. The compositional changes across layers I–IV were also quantitatively analyzed using a 1D compositional profile from a 13 nm cylindrical region of interest aligned perpendicular to the layers (Figure 2i). The interfaces between layers I–IV are marked with dashed lines in Figure 2i.

To further study how oxidation will proceed with longer exposures to oxygen, another APT needle was exposed to 10 mbar natural abundance O_2 at 300 °C for 30 min followed by APT analysis. The APT mass-to-charge spectra after 30 min oxidation are given in Figure S1 and S2 in the Supporting Information. Similar to what was observed after 5 min oxidation, in addition to the O^{+1} peak at 16 Da, a peak of OH^{+1} was observed at 17 Da and a peak of H_2O^{+1} was observed at 18 Da. The peak counts of 17 and 18 Da peaks were comparable (see Figure S2, Supporting Information). The four-layered structure was still observed based on the APT results of ion distribution after 30 min of oxidation (**Figure 3**a–d). The 2D compositional maps revealed comparable compositional changes across the layers, although there was some minor heterogeneity specifically in the Ni distribution in layer I. Interestingly, there was an increase in the thicknesses of the layers after 30 min exposure, where Fe rich oxide layer I increased from ≈2 to ≈4 nm, while the chromium-rich oxide layer II increased from ≈1.5 to ≈2 nm, when compared to 5 min exposure. The Ni-enriched layer still appeared to be ≈1 nm in thickness, like what was observed after 5 min of oxidation.

2.3. Complementary Ex Situ Multimodal Analysis of Oxide Layer Structure, Composition, and Oxidation State

To verify the structure of the oxide layers formed, a metallographically polished Fe18Cr14Ni bulk sample was also exposed

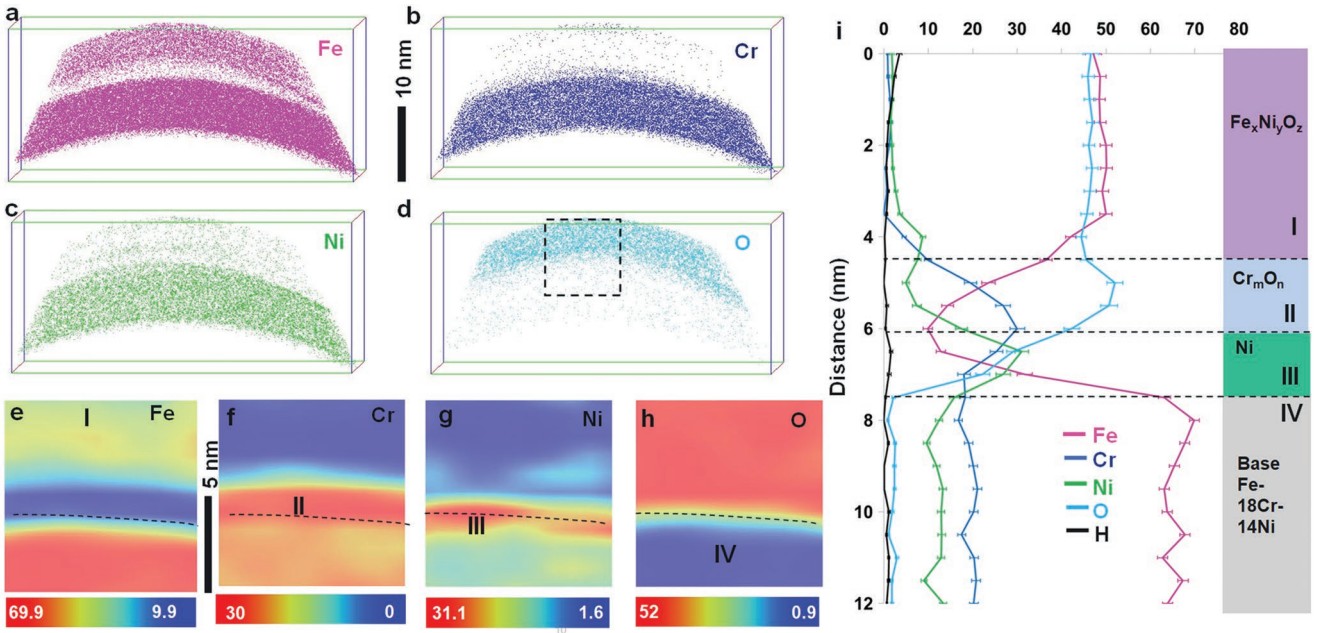

Figure 3. Oxide composition after 30 min oxidation at 300 °C in 10 mbar natural abundance O_2. Elemental distributions of a) Fe, b) Cr, c) Ni, and d) O revealed by APT after 300 °C, 30 min oxidation in natural-abundance oxygen. A 1 × 10 × 10 nm region of interest is marked by a dashed black rectangle from which 2D compositional maps were plotted to show the variation of e) Fe, f) Cr, g) Ni, and h) O across the oxide–metal interface. Individual compositionally distinct regions in the oxide and base alloys are marked by the numerals I–IV. The oxide–metal interface is demarcated using a dashed line in (e–h). i) 1D compositional profile showing the quantitative compositional changes from the oxide surface to the base alloy across the different layers.

to 10 mbar O_2 in the reactor chamber for 30 min at 300 °C (keeping the oxidation environments consistent with the in situ samples). Then cross-sectional TEM samples were extracted from the oxidized surfaces by site-specific focused ion beam (FIB) lift out. The scanning transmission electron microscopy (STEM) energy dispersive spectroscopy (EDS) maps from the cross-sectional TEM sample of the 30 min oxidized bulk alloy also revealed the Fe-rich surface oxide followed by the Cr rich oxide and a Ni enrichment at the oxide–metal interface as shown in **Figure 4**a–d and the EDS line profile in Figure 4e. The structure of the surface Fe-rich oxide layer was identified to be spinel Fe_3O_4 using high-angle annular dark-field (HAADF) STEM. The oxidation state of the oxide layers was then confirmed using XPS depth profiling. The background subtracted Fe 2p, Cr 2p, and Ni 2p XPS high resolution scans as a function of depth are shown in Figure 4g–i, respectively. Only spin orbit splitting peak of 3/2 is shown in these figures. All these elements show several multiplet peaks and satellite structures in their main XPS peaks. The XPS depth profiles additionally confirmed the Fe-rich surface oxide to be Fe_3O_4 followed by a layer of Cr-rich oxide as Cr_2O_3. Although XPS detected some minor amount of Ni in oxide layer, Ni was predominantly detected below the oxide layer present as Ni metal. The XPS results were cross-validated using XANES in total electron yield (TEY) mode. Similar observation of Ni enrichment at the oxide–metal interfaces was also reported in past publications that analyzed the environmental degradation of 304 stainless steels in pressurized water reactor environments.[37] The Fe L-edge, Ni L-edge, and Cr L-edge XANES results from the before and after oxidation conditions were compared with corresponding spectra from Fe_2O_3, Fe_3O_4, Cr_2O_3, and NiO standards (Figure 4j–l). The comparison of the XANES spectra confirmed Fe to be primarily present as Fe_3O_4 and Cr as Cr_2O_3 in the oxide layer. Ni however appeared to show some extent of oxidation to have +2 oxidation state which indicated that it may be also present in the top Fe_3O_4 oxide layer which agrees with the in situ APT observations after 5 and 30 min of oxidation.

2.4. In Situ APT with Double Stage Oxidation and ^{18}O Isotope Exposure

We then turned our attention to analyzing the diffusional mechanism responsible for the oxide growth at 300 °C using double step oxidation with an isotopically enriched $^{18}O_2$ exposure. An Fe18Cr14Ni alloy needle was transferred into the APT reactor chamber after the initial clean-up run and then exposed to 10 mbar O_2 (natural abundance) for 30 min at 300 °C to form the initial oxide layer. Then, the natural-abundance oxygen supply was shut off, and the chamber was evacuated and refilled with $^{18}O_2$ enriched oxygen gas for an additional 15 min of oxidation. The APT mass-to-charge spectra after the two stage oxidation are given in Figures S1 and S2 in the Supporting Information. After this two stage oxidation, it was observed that the peak count at 18 Da was significantly higher in intensity than the peak at 17 Da which clearly shows the intensity enhancement due to the ^{18}O exposure. Additionally, going by the previous observation of the comparable intensity of OH^{+1} peak at 17 Da and H_2O^{+1} peak at 18 Da after 5 and 30 min oxidation in natural abundance O_2, and given the peak count at 17 Da is very low after the double stage oxidation, the contribution of H_2O^{+1} to the peak at 18 Da after the double stage oxidation is

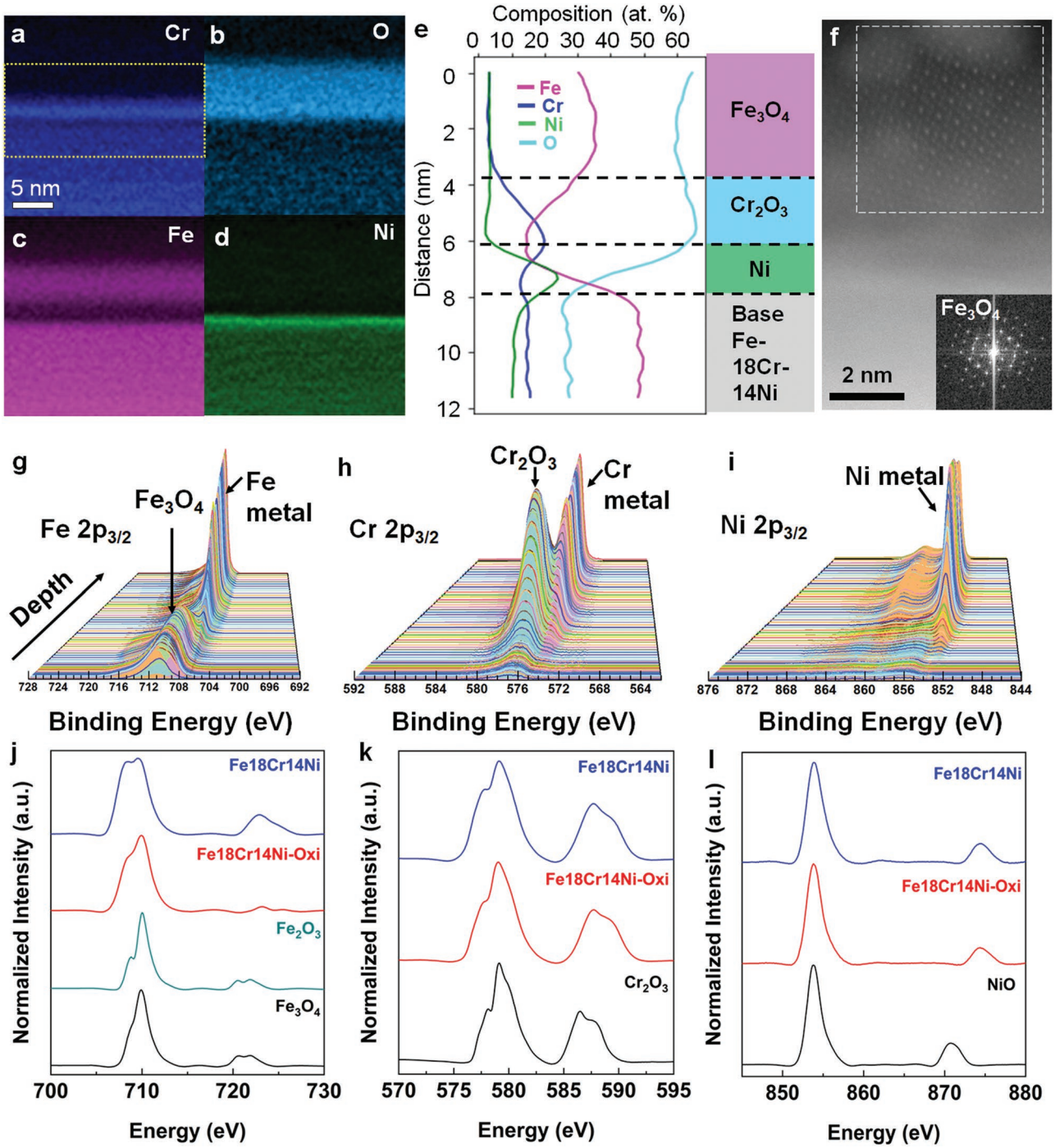

Figure 4. Ex situ multimodal characterization after 30 min oxidation at 300 °C in 10 mbar O_2. Cross-sectional scanning transmission electron microscopy energy dispersive spectroscopy (STEM-EDS) results after 300 °C 30 min oxidation of a polished bulk Fe18Cr14Ni alloy revealing distribution of a) Cr, b) O, c) Fe, and d) Ni across the oxide later. e) STEM-EDS compositional profile showing the compositional change across the oxide layers to base metal. f) High-angle annular dark-field (HAADF)-STEM image and corresponding fast Fourier transform (FFT) of the oxide layer revealing Fe_3O_4 structure. X-ray photoelectron spectroscopy (XPS) depth profile across confirming the presence of Fe_3O_4 near surface followed by Cr_2O_3 below. j–l) The total electron yield X-ray absorption near edge structure (XANES) of Fe, Cr, and Ni L edge of the Fe18Cr14Ni alloy before and after oxidation in comparison with corresponding XANES spectra from Fe_2O_3, Fe_3O_4, Cr_2O_3, and NiO standard oxides to verify the oxidation state of the different oxide layers.

considered to be minimal. The distribution of Fe, Cr, Ni, and O after this double-stage oxidation (**Figure 5**a–d) was also comparable to what was observed after 5 and 30 min of oxidation in Figures 2–4. However, due to the unique ability of APT to distinguish individual isotopes of oxygen at sub-nanometer spatial resolution in 3D, the ^{18}O peak at 18 Da was specifically resolved

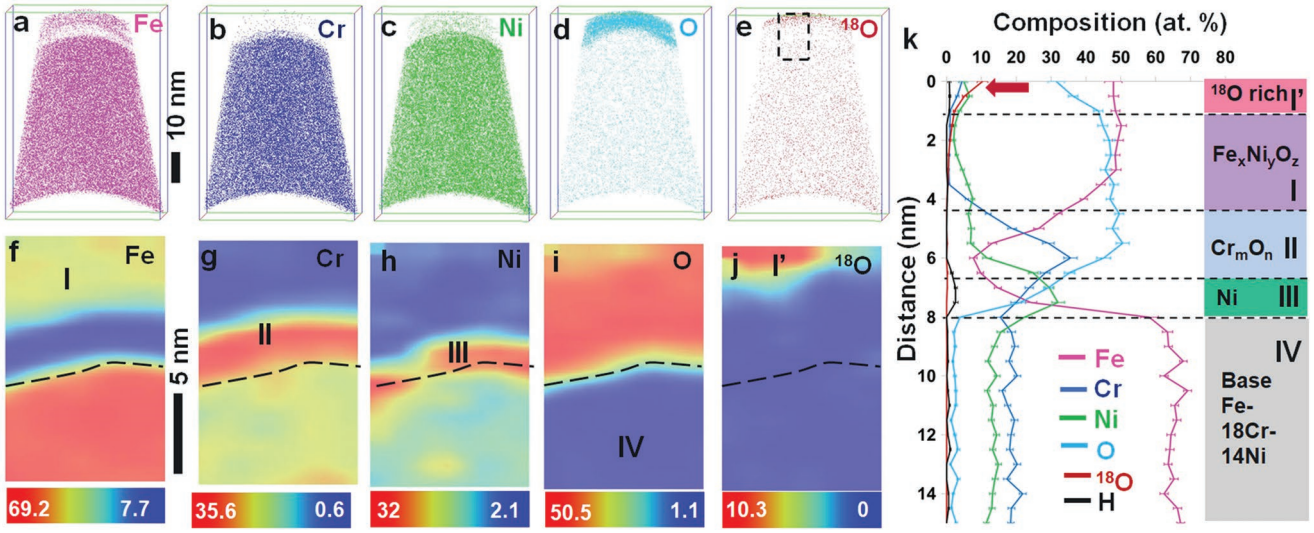

Figure 5. Compositional evolution after double stage oxidation. Elemental distribution after 30 min of oxidation at 300 °C in the presence of O_2 (with natural abundance) followed by a 15 min oxidation in isotopically enriched $^{18}O_2$: a) Fe, b) Cr, c) Ni, d) O, and e) ^{18}O ion distribution within the APT reconstruction. A $1 \times 10 \times 15$ nm^3 region of interest is marked by a dashed black rectangle from which 2D compositional maps were plotted to show the variation of f) Fe, g) Cr, h) Ni, i) O, and j) ^{18}O across the oxide–metal interface. Individual compositionally distinct regions in the oxide and base alloys are marked by I' and numerals I–IV. The oxide–metal interface is demarcated using a dashed line in (f)–(j). k) 1D compositional profile showing the quantitative compositional changes from the oxide surface to the base alloy across the different layers.

to be enriched very close to the top surface of the needle. The 2D concentration maps plotted using a $1 \times 10 \times 15$ nm^3 region of interest—given in Figure 5a–j—not only reveal the layers I–IV but also an ≈1 nm thick ^{18}O-enriched I' oxide layer very close to the top apex of the needle. This ^{18}O-rich I' oxide layer is also evident in the 1D compositional map given in Figure 5k. Interestingly, a slight thickening of the II and III layers is observed as well. The lack of a sharp interface for this ^{18}O-rich oxide layer and instead a diffused tail of ^{18}O concentration reaching up to 3 nm into oxide layer I indicates that the inward diffusion of ^{18}O is occurring through an ion-exchange mechanism with ^{16}O in the pre-existing oxide.

We then compared the oxygen compositional profiles after all three oxidation experiments in **Figure 6**, with 0 value in the distance *y*-axis denoting the surface of the APT reconstruction and the increasing distance going toward the base alloy. The horizontal dashed line marks the oxide–metal interface. Given that the ^{18}O-rich oxide layer (I') formed on the surface of the needle sample, it clearly indicates that ^{18}O in the second stage of oxidation did not diffuse through the oxide layer to reach the metal–oxide interface and form the new ^{18}O-rich oxide there. The presence of significant ^{16}O concentration in this ^{18}O rich surface oxide is because the ^{18}O enriched gas is a mixture of ^{18}O and natural abundant O_2. It was also observed that the maximum oxygen concentration in Cr_2O_3 decreased slightly from ≈52 at% after 30 min oxidation to ≈50.5 at% after the double stage oxidation. This decrease in maximum oxygen concentration is attributed to a difference in the Cr cation outward diffusion

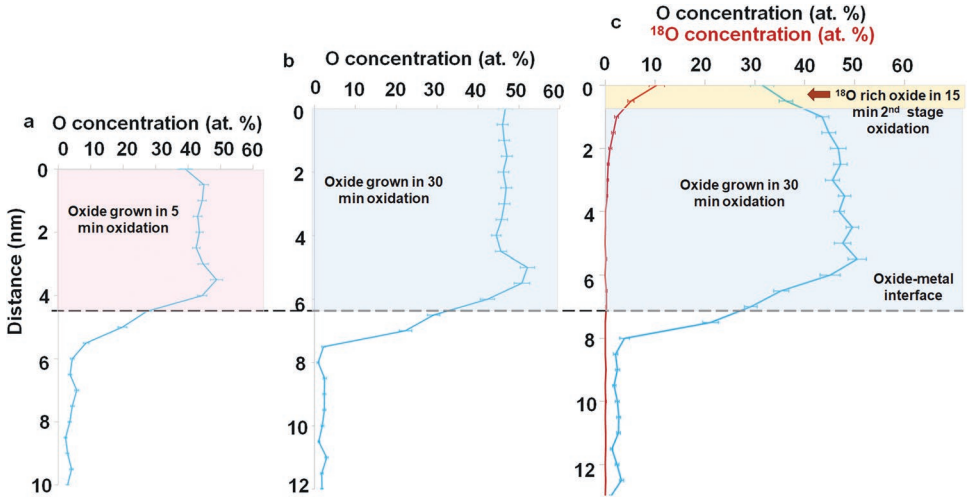

Figure 6. Time-resolved analysis of oxygen diffusion. Comparison of progressive change in oxygen composition across the different oxide layers during 5 min, 30 min, and double stage oxidation experiments at 300 °C.

and incorporation in to the Cr_2O_3 layer being faster than oxygen inward diffusion. In addition, there may be ^{16}O diffusion occurring within the oxides in between the Cr_2O_3 and the Fe_3O_4 layers which could also cause the change in oxygen concentration in the Cr_2O_3 layer.

To compare the diffusion of individual cations across the oxide–metal interface after 5, 30, and 45 min double stage oxidation, a one-to-one comparison of the distribution of Fe, Cr, and Ni compositional graphs are shown in **Figure 7**. Outward diffusion of Fe increased from 5 to 30 min and then during the 2nd stage ^{18}O oxidation to form Fe_3O_4 layer as evident in Figure 7a–c. Cr diffusion on the other hand is leading to a slight thickening of the Cr_2O_3 layer below Fe rich oxide Figure 7d–f. Marginal thickening of the Ni enriched layer occurred with increasing oxidation time Figure 7g–i. The peak Ni concentration in layer III and Ni concentration within layers I and II can be observed to increase when going from 5 to 30 to 45 min of oxidation. This observation points to continued outward diffusion of Ni through the Cr_2O_3 layer-II in to the top Fe_3O_4 layers I and I′ on continued oxidation (Figure 7g–i). To further understand the atomic scale diffusional mechanisms responsible for the multilayered oxide growth and Ni enrichment, these experimental observations were compared against computational simulations as described below.

2.5. Computational Simulations to Reveal Diffusion Mechanisms

Coupled Poisson–Nernst–Planck (PNP) transport kinetics model and classical density functional theory (cDFT) simulations offer further insight into the mechanism of oxidation in Fe18Cr14Ni alloy (**Figure 8**), indicating that oxide formation strongly depends on the formation energies and cation diffusivities in the alloy. The appearance of two oxide phases is directly related to significant differences in the formation energies of chromia, iron oxide, and nickel oxide. These formation energies reflect the energy gain upon the formation of the oxides and are equal to −11.7 eV for Cr_2O_3. −8.4 ± 0.1 eV for main polymorphs of iron oxides (Fe_2O_3 (Hematite, α-Fe_2O_3; Maghemite, γ-Fe_2O_3; ε-Fe_2O_3) and Fe_3O_4), and −2.5 eV for NiO, respectively.[38–40] The clear energetic preference for the formation of chromia and iron oxide is also reflected in the measured oxide composition in the interfacial region observed both in experiment and in simulations in this work. The differences in cation diffusivities for Fe, Cr, and Ni in the alloy, in turn, facilitate phase separation of the oxides and cation redistribution during oxidation. The measured activation energies for cation migration in Fe18Cr14Ni alloy were found to be largely independent of the relative Cr and Ni content and temperature. The diffusion coefficients of individual elements in Fe–Cr–Ni followed the relationship of $D_{Cr} > D_{Fe} > D_{Ni}$, with $D_{Cr}/D_{Ni} = 2.5$ and $D_{Fe}/D_{Ni} = 1.8$.[41] Mesoscale simulations predict that under these conditions iron oxide will form at the surface due to the abundance of Fe in the alloy and relatively high formation energy of iron oxide. The fastest diffusing Cr cations will diffuse about 2 nm inward to form Cr_2O_3, which has the highest absolute formation energy, in the subsurface region. It is noteworthy that Cr diffuses toward this region from both the surface and the bulk alloy side leaving a Ni-enriched region at the interface between chromia and the bulk alloy (Figure 8b). The simulated compositional profile from the oxide surface to bulk alloy reveal the formation of an Fe_3O_4 outer oxide with some Ni impurities, a Cr_2O_3 inner oxide, and Ni segregation at the oxide–metal interface (Figure 8b), all of which remarkably agrees with all the experimental results from this study. The periodic fluctuations in the simulated compositional profile of Fe and Ni within the oxide layers in Figure 8b result from the discreteness of the lattice sites and a 0.5 nm step size used for averaging the profiles. We note that Ni substitutional defects in Fe_3O_4 were mostly observed at the edges of the simulation box.

The experimental and computational results in this work agree closely with recent studies of commercial 304 stainless steels, where such two-stage oxidation experiments followed by time-of-flight-SIMS estimated cation diffusion coefficients in oxide, the cation diffusion coefficient (D_c) of 9×10^{-17} cm^2 s^{-1} which is substantially higher than the diffusion coefficient of oxygen (D_o) estimated to be $1.6–2\times10^{-17}$ cm^2 s^{-1}.[20] From this work, it is clear that once an initial oxide forms, the subsequent oxide growth rate will be primarily controlled by the diffusivity of Fe and Ni ions through the Cr-rich oxide layer II and through Ni enrichment at the oxide–metal interface (III). Cr from the base metal has to diffuse through the Ni-enriched oxide–metal interface (III) to reach the Cr-rich oxide layer (II). The continuing thickening of the Cr-rich oxide layer II and the Ni enrichment layer III at the oxide–metal interface means that the barrier for continued oxide growth can progressively increase with prolonged oxidation at 300 °C. Our results on model austenitic Fe18Cr14Ni alloy also agree with past studies of oxidation of commercial 304 and 316 stainless steels at temperatures up to 300 °C where a multilayer oxide consisting of an Fe-rich surface oxide and a Cr-rich inner oxide have been reported to form.[42] Our study reveals that the approach of two-step oxidation experiments of bulk alloys, where an initial layer of oxide was first formed by exposure of a bulk alloy sample to ^{16}O-rich oxygen or electrochemical exposure to acids, followed by exposure to $^{18}O_2$ isotopes for controlled times can now be used in the nanoscale in situ APT experiments to understand the oxidation mechanisms.[43] Thereby, our work extends this double stage oxidation approach to in situ APT, revealing 3D nanoscale distribution of elements during oxidation.

In the future, this spatially resolved nanoscale imaging of oxidation of austenite in an Fe18Cr14Ni alloy can be extended to further understand the changes in the diffusional mechanisms when oxidation is coupled with deformation or takes place in presence of hydrogen.[44] In the future this approach can also be extended to understand the influence of orientation on the nanoscale oxidation kinetics, like bulk corrosion studies in past that pointed to the influence of anisotropic surface energies on corrosion kinetics of different grain orientations in 316 stainless steels.[45] Additionally using results from such experiments of orientation influence on oxidation, the PNP-cDFT oxidation model will be further improved to account for the relative orientation relationship of the alloy grain and the different oxide layers in future. The in situ APT with two stage oxidation methodology described here can also be applied to the broader class of materials to study gas–surface reactions at nanoscale spatial resolution and with temporal resolutions as small as 1 min.

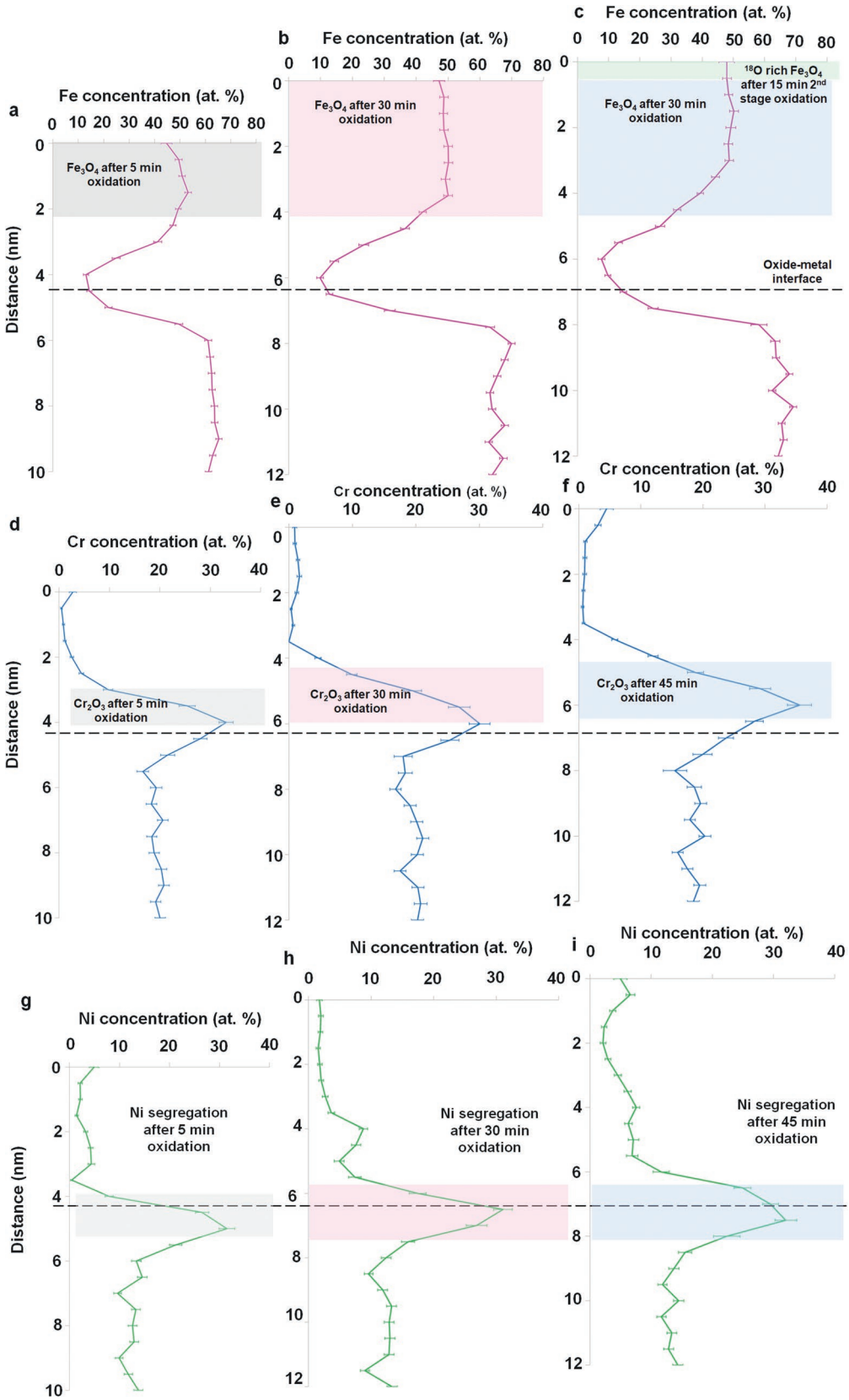

Figure 7. Time resolved analysis of cation diffusion. Comparison of cation diffusion across different oxide layers during 5 min, 30 min, and double stage oxidation experiments at 300 °C. a–c) Fe distribution, d–f) Cr distribution, and g–i) Ni distribution.

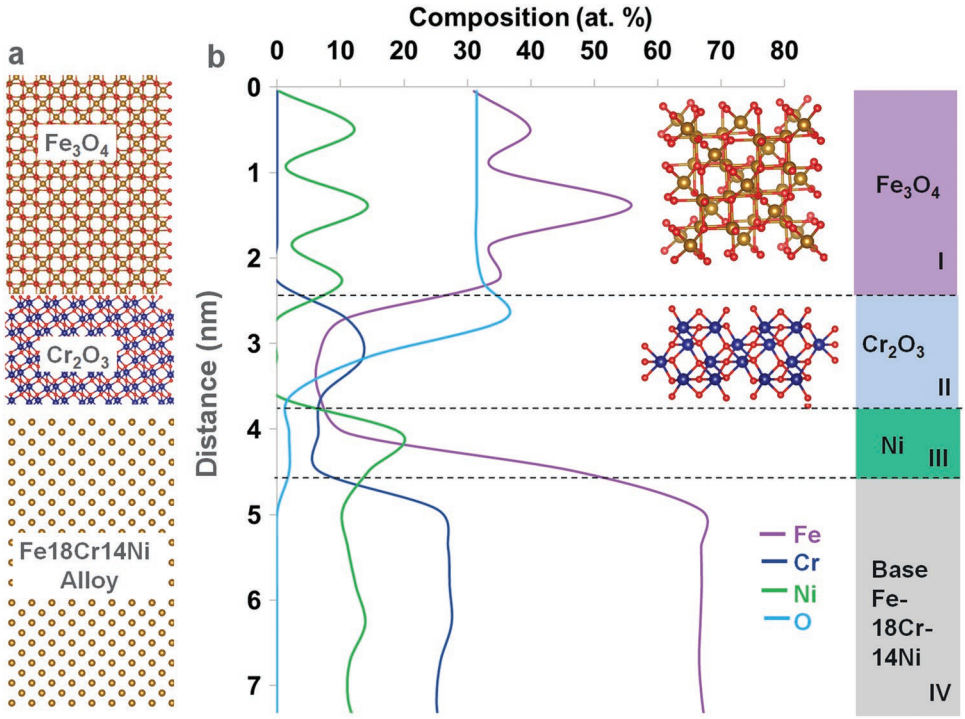

Figure 8. Computational analysis of the oxidation mechanism. a) Computational setup for the coupled Poisson–Nernst–Planck (PNP) transport kinetics model and classical density functional theory (cDFT) and b) predicted composition profile after oxidation showing the formation of Fe_3O_4, Cr_2O_3, and Ni segregation at the oxide–metal interface. The magnified structure of Fe_3O_4 and Cr_2O_3 are provided as inset. The layers are distinguished using roman numerals I–IV on the right side of the simulated compositional profile to highlight the agreement between this simulation and experimental results.

3. Conclusion

A novel in situ APT double stage oxidation experiment, multimodal ex situ characterization, and complementary mesoscale simulations were conducted to systematically analyze the diffusional phenomenon operating during oxidation of an austenitic Fe-18Cr-14Ni alloy. Oxidation at 300 °C for 5 and 30 min in natural-abundance oxygen allowed us to quantitatively analyze the changes in both composition and thickness of different oxide layers as a function of time. A double-stage oxidation experiment, which involved a first stage of exposing an Fe18Cr14Ni alloy to natural-abundance O_2 followed by a 15 min exposure to ^{18}O enriched O_2 revealed that the ^{18}O-rich oxide layer formed on top of the pre-existing oxide and not at the prior oxide–metal interface. This observation helped confirm that the outward diffusion of cations is the dominant diffusional mechanism. A secondary, less-dominant mechanism of inward diffusion of ^{18}O and ion exchange of ^{18}O with the ^{16}O within the preformed oxide was also observed. This approach of in situ APT with an ^{18}O isotopic tracer and complementary ex situ characterization by STEM-EDS, XPS depth profiling, XANES and mesoscale simulations opens new avenues for studying changes in the oxidation kinetics of alloys after subjecting them to deformation, irradiation, or other processing methods. This approach can also be invaluable for studying oxidation kinetics and oxygen transport phenomenon in broad classes of materials such as catalysts, automotive and nuclear structural materials, solid oxide fuel cells, and geological minerals and biominerals.

4. Experimental Section

Preparation of Model Fe18Cr14Ni Alloy: Fe–18 wt% Cr–14 wt% Ni alloys were induction melted from high-purity elements, then casted and homogenized by remelting five times. The alloys were subsequently cold rolled, resulting in a 50% reduction in area, and recrystallized to 3 mm thick sheets via recrystallization annealing at 900 °C for 4 h. The alloy sheet was then cut, mounted, and metallographically polished.

Microstructural Characterization of the Alloy before Oxidation: Oxford symmetry electron back scatter diffraction (EBSD) detector implemented on a Thermo Fisher scientific plasma focused ion beam (PFIB) system was used for the initial microstructural analysis of the alloy. Integrated AZtecHKL software was used to analyze the EBSD results. Synchrotron based high energy X-ray diffraction was conducted at the 11-ID-C beamline of the Advanced Photon Source (APS) at Argonne National Laboratory. A monochromatic X-ray beam with an energy of 105.7 keV (wavelength of 0.1173 Å) was used to collect the diffraction patterns of the alloy. The X-ray beam size was about 0.3 mm × 0.3 mm, and the detector was positioned 1.8 m away from the sample and calibrated using standard CeO_2 powder.

APT Sample Preparation and In Situ APT Procedure: Site-specific APT needles from the center of selected austenite grains were prepared using either a Thermo Fisher Hydra plasma FIB through a standard lift-out and annular milling process from the metallographically polished Fe18Cr14Ni alloy.[46] The APT needle samples were initially analyzed in a CAMECA LEAP 4000XHR APT system equipped with a 355 nm ultraviolet laser to understand the initial atomic distribution in the alloy. The APT analysis was stopped after collecting 250 000 or 500 000 ions and the needle sample was transferred into the environmental reactor chamber attached to the APT vacuum system.[26,29] The oxidation experiments were conducted at 300 °C while 10 mbar oxygen with either natural-abundance or isotopically enriched $^{18}O_2$ was flowed into the reactor chamber for specific time durations varying from 5 to 30 min. After the oxidation

experiments, the samples were promptly transferred to the APT analysis chamber. APT analysis of all samples was conducted under the same conditions to avoid any APT parameter-dependent changes in the results. The standard APT analysis parameters were 40 pJ laser pulse energy, 40 K specimen temperature, and a 200 kHz laser pulse repetition rate, while the evaporation rate was maintained at 0.005 atoms per pulse. The APT results were reconstructed using integrated visualization and analysis software (IVAS) 3.8. A high-resolution scanning electron microscope (SEM) image of the final APT needle sample was used for tip-profile reconstruction in IVAS for the initial cleanup run. The end diameter of the cleanup run was then used as input for a shank angle-based reconstruction of the APT data after oxidation.

Cross-Sectional STEM-EDS: TEM specimens were prepared using a Thermo Fisher Scientific Helios 5 Hydra DualBeam PFIB/SEM and an FEI Helios Nanolab FIB/SEM. STEM imaging and spectroscopy were performed using a Thermo Fisher Scientific Themis Z 60-300 S/TEM with an accelerating voltage of 300 kV and a convergence angle of 25 mrad. The high-resolution HAADF STEM images were collected with an annular detection range of 51–200 mrad. 25 frames of image with dwell time of 4 µs per pixel were postprocessed using a drift corrected frame integration method in Velox software to optimize the signal-to-noise and contrast. X-ray energy-dispersive spectroscopy (EDS) was collected to show the compositional map using Super-X G2 detector with a dwell time of 3 µs per pixel and 540 frames. EDS line profile was plotted perpendicular to metal–oxide interfaces and integrated over 50 pixels (3.5 nm).

XPS Depth Profiling of Oxidized Fe18Cr14Ni Alloy: XPS was used to measure the surface composition and chemical state of elements in as received and oxidized samples as a function of depth. XPS measurements were performed using a Nexsa Thermo Fisher Scientific spectrometer, using focused Al K_α monochromatic X-ray source (1486.6 eV) operated at 72 W and a high-resolution spherical mirror analyzer using 50 eV pass energy. The data acquisition was carried out using a 300 µm diameter X-ray beam and emitted photoelectrons were collected at the analyzer entrance slit normal to the sample surface. The chamber pressure was maintained at $\approx 5 \times 10^{-9}$ Torr during the measurements. All the XPS peaks were charge-referenced using O 1s binding energy of metal oxide at 530 eV. XPS data were analyzed by CasaXPS software using Shirley background correction. For depth profile measurement, 300 eV mono energetic argon ions were used. The ion beam was rastered about 1.2 mm × 1.2 mm area and the XPS measurements were performed at the center of the crater using 300 µm diameter X-ray beam. The Sputter depth scale was calibrated using Ta_2O_5 sputter rates.

XANES: The X-ray absorption near edge structure (XANES) study was performed at the Advanced Light Source (ALS), Lawrence Berkeley National Laboratory (LBNL). The Fe L-edge, Ni L-edge, and Cr L-edge were measured using bending magnet beamline 7.3.1. Energy ranges from 700 to 730, 570 to 595, and 845 to 880 eV for Fe, Cr, and Ni L-edge respectively. The edges were measured at the end-station with a total pressure of 5.0×10^{-8} Torr with a ring current of 500 mA. The incident photon flux was measured using a clean gold mesh upstream of the end-station. XANES data were collected at room temperature using TEY mode which measures the sample drain current resulting from photo and Auger electrons leaving the sample surface. The incident beam intensity was monitored (I_o) via the gold grid to normalize the total electron yield signal (I_I). Each final spectrum was an average of four scans. For comparison, asymmetric least squares smoothing baseline was performed and then renormalized using origin software.

Computational Method: Element profiles were simulated using the mesoscale model based on coupled PNP transport kinetics model and classical density functional theory (cDFT), which is used to calculate the free energies and free energy gradients driving atom migration and the formation of the oxides (see the Supporting Information for details). These include the free energies of Coulomb interactions, electrostatic correlations, hard sphere repulsion, and short-range interactions with the stationary (lattice) sites, which represent the equilibrium sites for matrix and minor elements in the crystal structure of the alloy and oxide.[47,48] A metal alloy/oxide interface is modeled in 3D as an array of interaction centers representing atomic positions of Fe, Cr, Ni, and O in the crystal lattices of the alloy (FCC), Fe_3O_4, and Cr_2O_3 oxide phases. The crystallographic vectors of the Fe FCC lattice are aligned along the Cartesian vectors of the simulation cell. An oxide slab of finite thickness (3 nm) resides at the planar surface of the metal alloy and the oxide slab is truncated at one end to represent the alloy/oxide interface at the leading edge of the oxidation front. The lattice of interaction centers in the oxide slab corresponds to a superposition of Fe atomic positions in Fe_3O_4 and Cr atoms in Cr_2O_3 oxides. The assumption was made that the oxygen concentration in the oxide region is sufficient for forming stoichiometric metal oxides with Fe_3O_4 and Cr_2O_3 structures. Simulations were performed at 300 °C matching the temperature employed in the experimental work. The role of interfaces was partially accounted for within the simulation model by using the atomistic structure of the interfaces with the preferential crystallographic alignment of the metal alloy and oxide phases. Specifically, based on ab initio simulations of the interface structures and experimental data,[49,50] <100> FeCrNi//<001> Cr_2O_3//<100> Fe_3O_4 orientations were considered. The development of space-charge regions and interface specific diffusion pathways were also treated within the model.

Supporting Information

Supporting Information is available from the Wiley Online Library or from the author.

Acknowledgements

This research was supported by the Department of Energy (DOE), Office of Science, Basic Energy Sciences, Materials Sciences and Engineering Division as a part of the Early Career Research Program FWP 76052. Theoretical simulations were supported by the Department of Energy, Office of Science, Basic Energy Sciences, Materials Sciences and Engineering Division FWP 56909. A.D. would like to acknowledge Bharat Gwalani for insightful peer review comments during PNNL information release process. The in situ APT was conducted using facilities at the Environmental Molecular Sciences Laboratory, a DOE national user facility funded by the Biological and Environmental Research Program and located at Pacific Northwest National Laboratory. PNNL is operated by Battelle for DOE under contract DE-AC05-76RL01830. The synchrotron based high energy X-ray diffraction used resources of the Advanced Photon Source, a U.S. DOE Office of Science User Facility operated for the DOE Office of Science by Argonne National Laboratory under Contract No. DE-AC02-06CH11357. The X-ray absorption near edge structure experiments used resources of the Advanced Light Source, a U.S. DOE Office of Science User Facility under contract no. DE-AC02-05CH11231.

Conflict of Interest

The authors declare no conflict of interest.

Data Availability Statement

The data that support the findings of this study are available from the corresponding author upon reasonable request.

Keywords

atom probe tomography, diffusion, material degradation, oxidation

Received: January 19, 2022
Revised: March 24, 2022
Published online: June 12, 2022

[1] Q. Zhu, Z. Pan, Z. Zhao, G. Cao, L. Luo, C. Ni, H. Wei, Z. Zhang, F. Sansoz, J. Wang, *Nat. Commun.* **2021**, *12*, 558.
[2] Y. Liu, F. Yang, Y. Zhang, J. Xiao, L. Yu, Q. Liu, Y. Ning, Z. Zhou, H. Chen, W. Huang, P. Liu, X. Bao, *Nat. Commun.* **2017**, *8*, 14459.
[3] M. Li, M. T. Curnan, M. A. Gresh-Sill, S. D. House, W. A. Saidi, J. C. Yang, *Nat. Commun.* **2021**, *12*, 2781.
[4] L. Luo, M. Su, P. Yan, L. Zou, D. K. Schreiber, D. R. Baer, Z. Zhu, G. Zhou, Y. Wang, S. M. Bruemmer, Z. Xu, C. Wang, *Nat. Mater.* **2018**, *17*, 514.
[5] L. Ma, B. Lynch, F. Wiame, V. Maurice, P. Marcus, *Corros. Sci.* **2021**, *190*, 109653.
[6] N. Badwe, X. Chen, D. K. Schreiber, M. J. Olszta, N. R. Overman, E. K. Karasz, A. Y. Tse, S. M. Bruemmer, K. Sieradzki, *Nat. Mater.* **2018**, *17*, 887.
[7] J. Shittu, M. Sadeghilaridjani, M. Pole, S. Muskeri, J. Ren, Y. Liu, I. Tahoun, H. Arora, W. Chen, N. Dahotre, S. Mukherjee, *npj Mater. Degrad.* **2021**, *5*, 31.
[8] C. Yan, Y. Xin, X.-B. Chen, D. Xu, P. K. Chu, C. Liu, B. Guan, X. Huang, Q. Liu, *Nat. Commun.* **2021**, *12*, 4616.
[9] H. Yang, L. Gong, H. Wang, C. Dong, J. Wang, K. Qi, H. Liu, X. Guo, B. Y. Xia, *Nat. Commun.* **2020**, *11*, 5075.
[10] F. Baiutti, F. Chiabrera, M. Acosta, D. Diercks, D. Parfitt, J. Santiso, X. Wang, A. Cavallaro, A. Morata, H. Wang, A. Chroneos, J. MacManus-Driscoll, A. Tarancon, *Nat. Commun.* **2021**, *12*, 2660.
[11] H. Wang, C. Chen, Y. Zhang, L. Peng, S. Ma, T. Yang, H. Guo, Z. Zhang, D. S. Su, J. Zhang, *Nat. Commun.* **2015**, *6*, 7181.
[12] Y. Zhao, C. Deng, D. Tang, L. Ding, Y. Zhang, H. Sheng, H. Ji, W. Song, W. Ma, C. Chen, J. Zhao, *Nat. Catal.* **2021**, *4*, 684.
[13] R. H. Smithies, Y. Lu, C. L. Kirkland, T. E. Johnson, D. R. Mole, D. C. Champion, L. Martin, H. Jeon, M. T. D. Wingate, S. P. Johnson, *Nature* **2021**, *592*, 70.
[14] J. W. Valley, A. J. Cavosie, T. Ushikubo, D. A. Reinhard, D. F. Lawrence, D. J. Larson, P. H. Clifton, T. F. Kelly, S. A. Wilde, D. E. Moser, M. J. Spicuzza, *Nat. Geosci.* **2014**, *7*, 219.
[15] J. W. Valley, *Geology* **2008**, *36*, 911.
[16] T. P. Almeida, T. Kasama, A. R. Muxworthy, W. Williams, L. Nagy, T. W. Hansen, P. D. Brown, R. E. Dunin-Borkowski, *Nat. Commun.* **2014**, *5*, 5154.
[17] R. A. Bentley, C. Knipper, *Archaeometry* **2005**, *47*, 629.
[18] W. H. Blades, P. Reinke, *ACS Appl. Mater. Interfaces* **2018**, *10*, 43219.
[19] C.-M. Wang, D. K. Schreiber, M. J. Olszta, D. R. Baer, S. M. Bruemmer, *ACS Appl. Mater. Interfaces* **2015**, *7*, 17272.
[20] L. Wang, S. Voyshnis, A. Seyeux, P. Marcus, *Corros. Sci.* **2020**, *173*, 108779.
[21] E. J. Kautz, D. K. Schreiber, A. Devaraj, B. Gwalani, *Materialia* **2021**, *18*, 101148.
[22] M. Bachhav, F. Danoix, B. Hannoyer, J. M. Bassat, R. Danoix, *Int. J. Mass Spectrom.* **2013**, *335*, 57.
[23] T. Kinno, M. Tomita, T. Ohkubo, S. Takeno, K. Hono, *Appl. Surf. Sci.* **2014**, *290*, 194.
[24] J. W. Valley, D. A. Reinhard, A. J. Cavosie, T. Ushikubo, D. F. Lawrence, D. J. Larson, T. F. Kelly, D. R. Snoeyenbos, A. Strickland, *Am. Mineral.* **2015**, *100*, 1355.
[25] T. C. Kaspar, S. D. Taylor, K. H. Yano, T. G. Lach, Y. Zhou, Z. Zhu, A. A. Kohnert, E. K. Still, P. Hosemann, S. R. Spurgeon, D. K. Schreiber, *Adv. Mater. Interfaces* **2021**, *8*, 2170050.
[26] S. V. Lambeets, E. J. Kautz, M. G. Wirth, G. J. Orren, A. Devaraj, D. E. Perea, *Top. Catal.* **2020**, *63*, 1606.
[27] E. J. Kautz, B. Gwalani, S. V. M. Lambeets, L. Kovarik, D. K. Schreiber, D. E. Perea, D. Senor, Y.-S. Liu, A. K. Battu, K.-P. Tseng, S. Thevuthasan, A. Devaraj, *npj Mater. Degrad.* **2020**, *4*, 29.
[28] S. V. Lambeets, T. Visart de Bocarmé, D. E. Perea, N. Kruse, *J. Phys. Chem. Lett.* **2020**, *11*, 3144.
[29] D. E. Perea, S. S. A. Gerstl, J. Chin, B. Hirschi, J. E. Evans, *Adv. Struct. Chem. Imaging* **2017**, *3*, 12.
[30] S. Lozano-Perez, J. Dohr, M. Meisnar, K. Kruska, *Metall. Mater. Trans. E* **2014**, *1*, 194.
[31] G. S. Was, in *Fundamentals of Radiation Materials Science: Metals and Alloys*, Springer, New York, NY **2017**, pp. 857–949.
[32] T. Shoji, Z. Lu, Q. Peng, in *Stress Corrosion Cracking* (Eds: V. S. Raja, T. Shoji), Woodhead Publishing, Cambridge, UK **2011**, pp. 245–272.
[33] P. L. Andresen, M. M. Morra, *Corrosion* **2008**, *64*, 15.
[34] P. L. Andresen, M. M. Morra, *J. Nucl. Mater.* **2008**, *383*, 97.
[35] K. Arioka, T. Yamada, T. Terachi, R. W. Staehle, *Corrosion* **2006**, *62*, 74.
[36] J. R. Scully, *MRS Bull.* **1999**, *24*, 36.
[37] K. Kruska, S. Lozano-Perez, D. W. Saxey, T. Terachi, T. Yamada, G. D. W. Smith, *Corros. Sci.* **2012**, *63*, 225.
[38] B. J. Boyle, E. G. King, K. C. Conway, *J. Am. Chem. Soc.* **1954**, *76*, 3835.
[39] W. M. Haynes, *CRC Handbook of Chemistry and Physics*, CRC Press, Boca Raton, FL, USA **2014**.
[40] A. Navrotsky, L. Mazeina, J. Majzlan, *Science* **2008**, *319*, 1635.
[41] S. J. Rothman, L. J. Nowicki, G. E. Murch, *J. Phys. F: Met. Phys.* **1980**, *10*, 383.
[42] L. Wang, A. Seyeux, P. Marcus, *Corros. Sci.* **2020**, *165*, 108395.
[43] S. N. Basu, J. W. Halloran, *Oxid. Met.* **1987**, *27*, 143.
[44] S. Moore, R. Burrows, D. Kumar, M. B. Kloucek, A. D. Warren, P. E. J. Flewitt, L. Picco, O. D. Payton, T. L. Martin, *npj Mater. Degrad.* **2021**, *5*, 3.
[45] S. Dong, X. Chen, E. C. La Plante, M. Gussev, K. Leonard, G. Sant, *Mater. Des.* **2020**, *191*, 108583.
[46] A. Devaraj, D. E. Perea, J. Liu, L. M. Gordon, T. J. Prosa, P. Parikh, D. R. Diercks, S. Meher, R. P. Kolli, Y. S. Meng, S. Thevuthasan, *Int. Mater. Rev.* **2018**, *63*, 68.
[47] M. L. Sushko, V. Alexandrov, D. K. Schreiber, K. M. Rosso, S. M. Bruemmer, *J. Chem. Phys.* **2015**, *142*, 214114.
[48] D. Meng, B. Zheng, G. Lin, M. L. Sushko, *Commun. Comput. Phys.* **2014**, *16*, 1298.
[49] V. Maurice, W. P. Yang, P. Marcus, *J. Electrochem. Soc.* **1998**, *145*, 909.
[50] M. Soldemo, M. Vandichel, H. Grönbeck, J. Weissenrieder, *J. Phys. Chem. C* **2019**, *123*, 16317.